PROCEEDINGS OF SPIE

High energy near- and far-field ptychographic tomography at the ESRF

Julio C. da Silva
Jan Haubrich
Guillermo Requena
Maxime Hubert
Alexandra Pacureanu
Leonid Bloch
Yang Yang
Peter Cloetens

SPIE.

High energy near- and far-field ptychographic tomography at the ESRF

Julio C. da Silva[a,*], Jan Haubrich[b], Guillermo Requena[b], Maxime Hubert[a], Alexandra Pacureanu[a], Leonid Bloch[a], Yang Yang[a], and Peter Cloetens[a]

[a]ESRF - The European Synchrotron, 38000 Grenoble, France
[b]Institute of Materials Research, German Aerospace Center (DLR), Linder Hhe, D-51147 Cologne, Germany

ABSTRACT

In high-resolution tomography, one needs high-resolved projections in order to reconstruct a high-quality 3D map of a sample. X-ray ptychography is a robust technique which can provide such high-resolution 2D projections taking advantage of coherent X-rays. This technique was used in the far-field regime for a fair amount of time, but it can now also be implemented in the near-field regime. In both regimes, the technique enables not only high-resolution imaging, but also high sensitivity to the electron density of the sample. The combination with tomography makes 3D imaging possible via ptychographic X-ray computed tomography (PXCT), which can provide a 3D map of the complex-valued refractive index of the sample. The extension of PXCT to X-ray energies above 15 keV is challenging, but it can allow the imaging of object opaque to lower energy. We present here the implementation and developments of high-energy near- and far-field PXCT at the ESRF.

Keywords: X-ray ptychography, ptychographic X-ray computed tomography, PXCT, near-field ptychography, far-field ptychography, high-energy x-rays, tomographic reconstruction methods, synchrotron X-ray imaging

1. INTRODUCTION

In computed X-ray tomography, 2D projections taken in multiple angular directions covering a $180\,°$-range are used to reconstruct a 3D image of an object by applying the inverse Radon transform to the projection data set.[1] The quality of the 3D images strongly depends on the quality of the 2D projections. Thus, different X-ray imaging techniques are used nowadays to improve the contrast and resolution of such projections: in-line holography,[2] propagation-based imaging,[3,4] and ptychography.[5,6] The common point in all those techniques is the use of coherent X-rays, like the one provided in the 3rd generation synchrotron sources.

One technique which has recently become very popular for its high resolving power and sensitivity is ptychography.[5–9] Such a technique can provide simultaneously the sample's complex-valued refractive index and the illumination, which allows taking into account inhomogeneities in the beam.[10,11] Actually, the frequency mixture of the structured beams would even improve the quality of the reconstructed images as previously discussed.[5,12,13] For years, part of the mathematical fundamentals of the technique remained poorly understood, but a new theoretical framework was recently proposed.[5] It uses the notion of decomposition of a signal into elementary signals proposed by D. Gabor[14] and the concept of frames,[15,16] which is the core of the theory of wavelets. Such a framework allows us deriving the sampling requirements and other experiments parameters in order to optimize the ptychographic scans even in challenging conditions as the use of high energy X-rays.

Ptychography at ID16A nano-imaging beamline of ESRF is implemented at high-energies ($17.05\,keV$ and $33.6\,keV$) with very high photon flux. This enables 2D and 3D high-resolution imaging of highly absorbing and bulky samples. With some changes in the experimental setup and very few changes in the phase-retrieval algorithms,[12,17,18] such a scanning microscopy technique can be implemented in either near- and far-field regimes. The redundancy of information offered by the overlapping of different scanning spots and oversampling in the detector plane is explored for the ptychographic phase-retrieval procedure.[5,6] Both variants are currently available at ID16A nanoimaging beamline.

---

*Correspondence to J.C.d.S.: E-mail: jdasilva@esrf.fr, Telephone: +33 (0)4 76 88 27 72

Finally, the combination of ptychography with tomography gives rise to the ptychographic X-ray computed tomography (PXCT) technique.[9,19,20] PXCT is part of the most recent developments on the ID16A beamline of ESRF. It can provide a 3D map of the complex-valued refractive index ($n(\vec{r}) = 1 - \delta(\vec{r}) + i\beta(\vec{r})$) of the sample with the high spatial resolution and high sensitivity. We can obtain the electron density of a sample from the refractive index decrement, $\delta(\vec{r})$, and its linear attenuation coefficient from the absorption index, $\beta(\vec{r})$. Therefore, PXCT is a fully quantitative technique.[7,8] At the ID16A beamline, high-energy PXCT has already been applied to many problems in life and material sciences. We present here the developments in high-energy PXCT at ID16A beamline as well as possibilities of applications in materials sciences. We outline the pipeline used to process the data and obtain the high-quality tomography.

2. HIGH-ENERGY PTYCHOGRAPHY

In the implementation of far-field ptychography, the sample is scanned with a spatially localized beam and overlapping adjacent scanning spots. An interference speckled-pattern, related to the Fourier transform of the probed part of the sample, is recorded at the detector plane for each scan position in the Fraunhofer regime.[5,6,21] In this case, the resolution of the retrieved image is independent of the focus. In the near-field ptychography, transverse diversity and redundancy needed for the phase retrieval are induced by transversely translating the sample within a coherent and structured beam, which is typically larger than the sample.[12] An in-line hologram is recorded on the detector, in the holographic Fresnel regime, for each sample position. Due to the small focal spot provided at the ID16A beamline, we usually record magnified holograms in order to obtain high-resolution images. In both variants of ptychography, the images are reconstructed by iterative algorithms which try to reinforce the consistency between the different scanning positions and the acquired data for each of them, as well as the consistency among the different overlapping scanned regions. Software tools are already available to the community for such reconstructions, and at the ID16A beamline we use the Python package Ptypy.[17]

One of the main requirements for ptychography is the high degree of coherence of the X-ray beam impinging into the sample. The higher the energy, the harder to obtain such a coherence. In third generation synchrotron sources, the beam is not coherent when it goes out of the ring. Thus, coherence filtering is needed and is implemented by creating a secondary source, which can be a pair of slits at a distance L upstream the sample. The degree of transverse coherence ξ_t can be estimated as $\xi_t = \lambda L/(2s)$, where λ is the wavelength and s is the aperture of such a secondary source. We can notice that L needs to be relatively long for high energies (short wavelengths) in order to recover enough coherence. This is exactly what it is done at ID16A nano-imaging beamline of ESRF, where the sample is about $185\,m$ from the source and about $145\,m$ from the secondary source. Such a long beamline provides a relatively high degree of coherence of the X-ray beam at the sample position for the ptychography experiments at two discrete energies: $17.05\,keV$ and $33.6\,keV$.

Secondly, the sampling of ptychographic data requires that there are at least two pixels in the detector for each speckle in the far-field regime or at least two pixels for each Fresnel fringe in the near-field regime. Since the size of a speckle or a Fresnel fringe is smaller as the X-ray energy gets higher, one needs an efficient detector with relatively small pixel. At ID16A beamline, we use indirect detection systems as the FReLoN CCD cameras,[22] which enables experiments with high photon flux and high energies provided by the beamline. Furthermore, the criterion for optimizing the overlap, the illumination size, scan pattern, sample-to-detector distance, and the detector pixel size have been previously published.[5,12]

Recently, ptychography at ID16A has successfully carried out using $33.6\,keV$ X-ray photons, which is currently the world's highest energy in which ptychography has been performed.[10] Such achievement opens new possibilities for the application of high-energy PXCT to important scientific problems where the sample is bulky or opaque to lower energies.

3. THE PRE-PROCESSING STEPS

Before the actual tomographic reconstruction, there are several pre-processing steps to follow: removal of the linear phase ramp and phase offset, phase unwrapping when necessary, vertical and horizontal registration of the projections. Those steps are described in the following subsections.

3.1 Linear phase ramp removal and phase offset

In the ptychographic reconstruction, an ambiguity on the linear phase term arises from the fact that both the object and illumination are simultaneous retrieved from data taken at different scanning positions. This ambiguity is intrinsic to ptychography. Since the wavefield past the sample is assumed to be the multiplication of the complex-values functions of the object and the of the illumination, a linear phase ramp multiplying the object can be compensated by a linear phase ramp of opposite sign multiplying the illumination. Additionally, any information about an overall phase shift provided by the sample is lost because we can only measure intensity patterns. Thus, the reconstructions should be corrected by an additive constant and linear phase terms. At ID16A beamline, we used a method proposed by Guizar-Sicairos *et al.*[20] for those corrections. A priori information of a known part of the sample is required in order to estimate the additive phase constant and we typically use a region of air as reference.

3.2 Phase unwrapping

Ptychography is a technique which allows the phases to go over several π's.[7] However, the phases are retrieved using expression involving arctangent, i.e, extracted from a trigonometric function $e^{i\varphi}$, where φ is the phase. Therefore, the resulting phases are given in modulo 2π and discontinuities appear when the phases reach π or $-\pi$. The unwrapping procedure consists in resolving such discontinuities and restoring the desired continuous phase function. At ESRF, we typically used algorithms like the classical Goldstein's[23] and Flynn's[24] algorithms or others like the one implemented the Python package Scikit-image[25] proposed by Herraez et al.[26] The latter is more often used because it is faster than the first two ones. Nevertheless, for the more complicated cases we use the Goldstein's algorithm and, when the result is still not satisfactory, we use Flynn's algorithm, which is quite slow, but efficient.

3.3 Registration of the projections

In PXCT, the sample is transversely displaced by piezo motors for each projections over a rotation of 180 °. The long experiments in addition to imprecisions of the motors will cause misalignments of the projections. In order to reconstruct high-resolution 3D images using tomography, one has to register such a set projections with less then one pixel precision. At ID16A beamline, we align the projections independently in the vertical and horizontal directions with sub-pixel precision using algorithms adapted to the information contained in the ptychographic projections.[20]

3.3.1 Vertical registration

For vertical alignment of the projections, we use the phase-contrast projections obtained by ptychography and the Helgason-Ludwig consistency condition.[27, 28] Such a condition states that:

$$\int \mathcal{R}(f)(\theta, p)dp = \iint f(x, z)dxdz, \tag{1}$$

where $\mathcal{R}(f)$ is the Radon transform (sinogram) of the $2D$ function $f(x, z)$, with $f(x, z)$ being the 2D sub-space of the 3D function $f(x, y, z)$, p is the radial coordinate of the sinogram, θ is the projection angle, z is the direction of the X-ray beam, and the x, y-coordinates define the plan of the projection.

Equation (1) is basically the Plancherel's theorem for the Radon transform[29] and states that the integral of any projection along p is independent of the angle θ. Thus, we can define the vertical mass distribution $vmd_\theta(y)$ as the integration of the phase along horizontal direction x of the projections:[20]

$$vmd_\theta(y) = \int \varphi_\theta(x, y)dx = -\frac{2\pi}{\lambda} \iint \delta(x\cos\theta - z\sin\theta,\, y,\, z\cos\theta + x\sin\theta)dxdz, \tag{2}$$

where $\varphi_\theta(x, y)$ represents the phase-contrast projections and $\delta(.)$ is the refractive index decrement of the sample. Therefore, based on this, Guizar-sicairos *et al.*[20] derived an iterative alignment approach to maximize the correlation of the vertical mass distributions of the sample and align the projections vertically. This has the advantage that we only use a 1D function for the alignment rather than using the complete 2D images. At ESRF, we implemented such algorithm in Python and we use for the alignment of the near- and far-field ptychography projections.

3.3.2 Horizontal registration

We perform the horizontal alignment of the projections using the tomographic consistency condition, which states that there is an unique relationship between the sinogram and the reconstructed tomographic slice.[30–32] Based on such a condition and on previously published algorithms,[31, 32] Guizar-sicairos *et al.*[30] proposed an improved iterative alignment in which, a tomographic reconstruction of the misaligned projections is obtained following by a forward Radon transform to obtain the sinogram from that reconstruction. The consistency condition states that such a sinogram will be the original sinogram only if both are consistent with a 3D representation. This will not be the case given that the projections are misaligned. Thus, we can use that consistency to robustly refine the misaligned sinogram to match the sinogram obtained from the reconstruction at each iteration to align the projections. For the inverse Radon transform, we use the modified filtered-back-projection algorithm described in the next section.

4. THE TOMOGRAPHIC RECONSTRUCTION

There are several tomographic reconstruction algorithms, and filtered-back-projection (FBP)[33] is the most used one. Since it is not iterative, it does not present problems of convergence and it is robustly fast. In addition, it allows to apply frequency cutoffs and filters to the data. At ESRF we use a modified version of FPB which calculates the tomographic slices from the derivatives of the projections. By modifying the filter, such modified FBP can even be insensitive to the phase wrapping[20] and, therefore, it is of great interest to PXCT reconstructions.

4.1 Modified Filtered Back Projection (FBP) algorithm

The standard FBP algorithm implements the reconstruction by:[20]

$$-\frac{2\pi u}{\lambda}\delta(\vec{r}) = \int_0^\pi \mathcal{F}_f^{-1}\{\,|\,f\,|\,\mathcal{F}_x\,[\varphi_\theta(x,y)]\,\}d\theta, \tag{3}$$

where $\mathcal{F}[.]$ is the forward 1D Fourier transform, $\mathcal{F}^{-1}\{.\}$ is the inverse Fourier transform, u is the voxel size, and $|\,f\,|$ is the ram-lak filter applied to the projections. By using the derivative property of the Fourier transform, $\mathcal{F}_x\{\partial\varphi/\partial x\} = i2\pi u\mathcal{F}_x\{\varphi\}$, we can rewrite the equation (3) as:[20]

$$-\frac{2\pi u}{\lambda}\delta(\vec{r}) = \int_0^\pi \mathcal{F}_f^{-1}\left\{\frac{1}{i2\pi\ sgn(f)}\mathcal{F}_x\left\{\frac{\partial\varphi_\theta(x,y)}{\partial x}\right\}\right\}d\theta, \tag{4}$$

where $\partial\varphi_\theta(x,y)/\partial x$ is the derivative of the phase projections and $sgn(.)$ is the signal function. The new filter is now $1/[i2\pi\ sgn(f)]$, which is sometimes referred as Hilbert filter. For the PXCT reconstructions at ESRF, we used such a modified version of FBP.

5. EXPERIMENTAL RESULTS

PXCT is routinely offered at ID16A beamline of ESRF in both near- and far-field regimes and has been applied to a wide range of scientific problems in life and material sciences. A recent example of applications of near-field PXCT to fuel cells was demonstrated in a previous work[19] and another example of far-field PXCT application to materials research is shown below.

5.1 Applications to materials science

Far-field PXCT was recently applied to study interfaces between metals and polymer for applications in aerospace industry. The sample was made of a titanium alloy bounded to a polymer and a deposition layer of platinum on the top coming from the focused-ion-beam (FIB) preparation. The experiments were performed at ID16A beamline using an energy of $17.05\,keV$ and $1\,\%$ bandwidth. We used a binary acquisition strategy[34] with 4 interlaced sub-tomograms acquired over a range of $180\,°$. 360 projections were acquired with angular step of $0.5\,°$. Each projection was obtained from a far-field ptychography experiment with a beam size of $1.4\,\mu m$ at the sample position and scanning step size of $600\,nm$. The coherent diffraction patterns were acquired with a FReLoN CCD detector[22] with effective pixel size of $19.6\,\mu m$ located at $1.2\,m$ downstream the sample. The

exposure time in each position was $0.5\,s$ and the beam divergence past the KB mirrors was $0.6\,mrad$. Thence, we can estimate the sampling ratio, which was $1/\alpha\beta\ =\ 7.6$, where $\alpha\ =\ 0.43$ is the ratio step-size/beam-size and $\beta\ =\ 0.31$ is the inverse of the oversampling factor in the reciprocal space.[5] This indicates that the sampling requirements were respected. The ptychographic phase-retrieval was carried out using the package Ptypy[17] and tomographic processing steps were performed using inhouse developed Python scripts follow the steps described in the sections above.

Figure 1 displays the results of the PXCT data processing. Figure 1(a) shows an axial slice, without any post-processing, of the volume where we can distinguish the different materials. The voxel size is $13.06\,nm$ and the diameter of the sample is $18.3\,\mu m$. Figure 1(b) presents the 3D rendering of the volume where the different materials are indicated: blue for a protecting platinum layer used during sample preparation, cyan for the polymer layer, gray for the titanium. We have also identified some porosity regions formed during processing of the titanium surface. This example is an important scientific case where high-energy X-rays PXCT represents a powerful imaging technique.
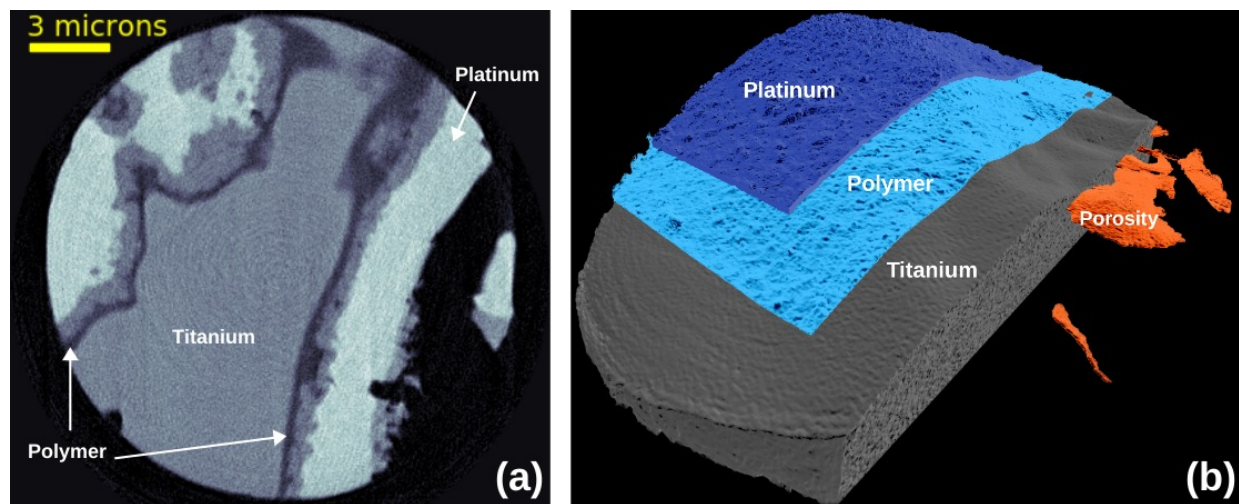

Figure 1. Hybrid metal-polymer material. (a) An axial slice of the tomographic volume obtained by PXCT. (b) 3D rendering of the volume. The different material phases are indicated. The voxel size is $13.06\,nm$ and the diameter of the cylinder is $18.3\,\mu m$.

6. CONCLUSIONS

We described here the implementation of near- and far-field ptychography at ID16A nano-imaging beamline of ESRF. We tackled the challenge of performing such a technique with high-energy X-rays ($17.05\,keV$ and $33.6\,keV$) and sufficiently high degree of coherence required by ptychography. This will therefore allow better resolved 3D imaging of highly absorbing and thick samples, commonly found in metallurgy, energy related materials or packaged semiconductor devices, for example. The PXCT benefits from the high flux to image the object with enough sensitivity, i.e., high sensitivity to weak variations of electron density of a sample. Several applications are already taking advantage of the high-energy PXCT at ESRF as shown in section 5.1 and figure 1. We also showed that the capability of ptychography to provided the complex-valued refractive index of the sample opens new opportunities for methodological developments in terms of tomographic data processing.

ACKNOWLEDGMENTS

registration and tomographic reconstruction algorithms and to T. Elberfeld for the implementation of Goldstein's and Flynn's algorithms.

REFERENCES

[1] Natterer, F., [*The Mathematics of Computerized Tomography*], Society for Industrial and Applied Mathematics, Philadelphia, PA, USA (2001).

[2] Cloetens, P., Ludwig, W., Baruchel, J., Dyck, D. V., Landuyt, J. V., Guigay, J. P., and Schlenker, M., "Holotomography: Quantitative phase tomography with micrometer resolution using hard synchrotron radiation x rays," *Appl. Phys. Lett.* **75**(19), 2912–2914 (1999).

[3] Cloetens, P., Ludwig, W., Baruchel, J., Guigay, J.-P., Pernot-Rejmnkov, P., Salom-Pateyron, M., Schlenker, M., Buffire, J.-Y., Maire, E., and Peix, G., "Hard x-ray phase imaging using simple propagation of a coherent synchrotron radiation beam," *J. Phys. D: Appl. Phys* **32**(10A), A145 (1999).

[4] Snigirev, A., Snigireva, I., Kohn, V., Kuznetsov, S., and Schelokov, I., "On the possibilities of xray phase contrast microimaging by coherent highenergy synchrotron radiation," *Rev. Sci. Instrum.* **66**(12), 5486–5492 (1995).

[5] da Silva, J. C. and Menzel, A., "Elementary signals in ptychography," *Opt. Express* **23**(26), 33812–33821 (2015).

[6] Thibault, P., Dierolf, M., Menzel, A., Bunk, O., David, C., and Pfeiffer, F., "High-resolution scanning x-ray diffraction microscopy," *Science* **321**(5887), 379–382 (2008).

[7] da Silva, J. C., Trtik, P., Diaz, A., Holler, M., Guizar-Sicairos, M., Raabe, J., Bunk, O., and Menzel, A., "Mass density and water content of saturated never-dried calcium silicate hydrates," *Langmuir* **31**(13), 3779–3783 (2015).

[8] da Silva, J. C., Mader, K., Holler, M., Haberthür, D., Diaz, A., Guizar-Sicairos, M., Cheng, W.-C., Shu, Y., Raabe, J., Menzel, A., and vanBokhoven, J. A., "Assessment of the 3d pore structure and individual components of preshaped catalyst bodies by x-ray imaging," *ChemCatChem* **7**(3), 413–416 (2015).

[9] Dierolf, M., Menzel, A., Thibault, P., Schneider, P., Kewish, C. M., Wepf, R., Bunk, O., and Pfeiffer, F., "Ptychographic x-ray computed tomography at the nanoscale," *Nature* **467**(7314), 436–439 (2010).

[10] da Silva, J. C., Pacureanu, A., Yang, Y., Bohic, S., Morawe, C., Barrett, R., and Cloetens, P., "Efficient concentration of high-energy x-rays for diffraction-limited imaging resolution," *Optica* **4**(5), 492–495 (2017).

[11] Thibault, P., Dierolf, M., Bunk, O., Menzel, A., and Pfeiffer, F., "Probe retrieval in ptychographic coherent diffractive imaging," *Ultramicroscopy* **109**(4), 338 – 343 (2009).

[12] Stockmar, M., Cloetens, P., Zanette, I., Enders, B., Dierolf, M., Pfeiffer, F., and Thibault, P., "Near-field ptychography: phase retrieval for inline holography using a structured illumination," *Sci. Rep.* **3**, 1927 (2013).

[13] Guizar-Sicairos, M., Holler, M., Diaz, A., Vila-Comamala, J., Bunk, O., and Menzel, A., "Role of the illumination spatial-frequency spectrum for ptychography," *Phys. Rev. B* **86**, 100103 (2012).

[14] Gabor, D., "Theory of Communication," *J. IEE* **93**(26), 429–457 (1946).

[15] Daubechies, I., Grossmann, A., and Meyer, Y., "Painless nonorthogonal expansions," *J. Math. Phys* **27**(5), 1271–1283 (1986).

[16] Duffin, R. and Schaeffer, A., "A class of nonharmonic fourier series," *Trans. Am. Math. Soc.* **72**, 341–366 (1952).

[17] Enders, B. and Thibault, P., "A computational framework for ptychographic reconstructions," *Proc. R. Soc. A* **472**(2196), 20160640 (2016).

[18] Thibault, P. and Menzel, A., "Reconstructing state mixtures from diffraction measurements," *Nature* **494**(7435), 68–71 (2013).

[19] Stockmar, M., Hubert, M., Dierolf, M., Enders, B., Clare, R., Allner, S., Fehringer, A., Zanette, I., Villanova, J., Laurencin, J., Cloetens, P., Pfeiffer, F., and Thibault, P., "X-ray nanotomography using near-field ptychography," *Opt. Express* **23**(10), 12720–12731 (2015).

[20] Guizar-Sicairos, M., Diaz, A., Holler, M., Lucas, M. S., Menzel, A., Wepf, R. A., and Bunk, O., "Phase tomography from x-ray coherent diffractive imaging projections," *Opt. Express* **19**, 21345–21357 (Oct 2011).

[21] Rodenburg, J. M., Hurst, A. C., Cullis, A. G., Dobson, B. R., Pfeiffer, F., Bunk, O., David, C., Jefimovs, K., and Johnson, I., "Hard-x-ray lensless imaging of extended objects," *Phys. Rev. Lett.* **98**, 034801 (2007).

[22] Labiche, J.-C., Mathon, O., Pascarelli, S., Newton, M. A., Ferre, G. G., Curfs, C., Vaughan, G., Homs, A., and Carreiras, D. F., "Invited article: The fast readout low noise camera as a versatile x-ray detector for time resolved dispersive extended x-ray absorption fine structure and diffraction studies of dynamic problems in materials science, chemistry, and catalysis," *Review of Scientific Instruments* **78**(9), 091301 (2007).

[23] Goldstein, R. M., Zebker, H. A., and Werner, C. L., "Satellite radar interferometry: Two-dimensional phase unwrapping," *Radio Sci.* **23**(4), 713–720 (1988).

[24] Flynn, T. J., "Two-dimensional phase unwrapping with minimum weighted discontinuity," *J. Opt. Soc. Am. A* **14**(10), 2692–2701 (1997).

[25] van der Walt, S., Schönberger, J. L., Nunez-Iglesias, J., Boulogne, F., Warner, J. D., Yager, N., Gouillart, E., Yu, T., and the scikit-image contributors, "scikit-image: image processing in Python," *PeerJ* **2**, e453 (2014).

[26] Herráez, M. A., Burton, D. R., Lalor, M. J., and Gdeisat, M. A., "Fast two-dimensional phase-unwrapping algorithm based on sorting by reliability following a noncontinuous path," *Appl. Opt.* **41**(35), 7437–7444 (2002).

[27] Ludwig, D., "The radon transform on euclidean space," *Comm. Pure Appl. Math.* **19**(1), 49–81 (1966).

[28] Helgason, S., "The radon transform on euclidean spaces, compact two-point homogeneous spaces and grassmann manifolds," *Acta Math.* **113**, 153–180 (1965).

[29] Durrani, T. S. and Bisset, D., "The radon transform and its properties," *Geophysics* **49**(8), 1180–1187 (1984).

[30] Guizar-Sicairos, M., Boon, J. J., Mader, K., Diaz, A., Menzel, A., and Bunk, O., "Quantitative interior x-ray nanotomography by a hybrid imaging technique," *Optica* **2**(3), 259–266 (2015).

[31] Mayo, S., Miller, P., Gao, D., and Sheffield-Parker, J., "Software image alignment for x-ray microtomography with submicrometre resolution using a sem-based x-ray microscope," *J. Microsc.* **228**(3), 257–263 (2007).

[32] Dengler, J., "A multi-resolution approach to the 3d reconstruction from an electron microscope tilt series solving the alignment problem without gold particles," *Ultramicroscopy* **30**(3), 337–348 (1989).

[33] Bracewell, R. and Riddle, A., "Inversion of fan-beam scans in radio astronomy," *Astrophys. J.* **150**, 427–434 (1967).

[34] Kaestner, A., Münch, B., Trtik, P., and Butler, L., "Spatiotemporal computed tomography of dynamic processes," *Optical Engineering* **50**(12), 123201–123201–9 (2011).